ChemComm

COMMUNICATION

Cite this: *Chem. Commun.*, 2021, **57**, 6503

Received 30th January 2021, Accepted 20th May 2021

DOI: 10.1039/d1cc00557j

rsc.li/chemcomm

Enhanced ion transport in Li_2O and Li_2S films†

Simon Lorger, Kai Narita, Robert Usiskin* and Joachim Maier

Films of Li_2O and Li_2S grown by sputter deposition exhibit Li^+ conductivity values at room temperature which are enhanced by 3–4 orders of magnitude relative to bulk samples. Possible mechanisms are discussed. The results may help explain the ion transport pathway through passivation layers containing these chalcogenides in batteries.

Lithium oxide (Li_2O) and lithium sulfide (Li_2S) are frequently encountered in batteries. They typically form as part of a solid–electrolyte interphase (SEI) passivation layer when a low-voltage anode reduces an electrolyte that contains the elements oxygen or sulfur.[1–3] They are also an important reaction product in conversion electrodes based on oxides,[4] oxygen,[5] nitrates,[6] sulfides,[4] sulfur,[7] and so on. The solid-state ion transport rates within the Li_2O and Li_2S can limit battery performance, yet the rates are not well-understood, partly because many phases are involved. To deconvolute the contributions and identify the rate-limiting mechanisms, it is valuable to study the individual materials in isolation.

The defect chemistry in bulk samples of Li_2O and Li_2S was characterized previously.[8,9] Both compounds take the antifluorite structure and are well described by a defect chemical model based on Frenkel disorder. The Li^+ conductivity can vary by orders of magnitude depending on doping, but the ionic defect mobilities are low, so even under favorable doping conditions, equilibrated bulk samples show an ionic conductivity at 25 °C below 10^{-10} S cm^{-1}. This limit is 1–3 orders of magnitude lower than the ionic conductivity estimated for typical SEI layers containing Li_2O or Li_2S,[1,2,10] as mentioned previously[8,9] and discussed in more detail below. The disparity suggests that ion transport in SEI layers cannot be explained by simple models that consider only point defects in bulk-like Li_2O and Li_2S. However, higher-dimensional defects such as grain boundaries, dislocations, interfaces, and amorphous content sometimes provide faster transport paths, and such defects are often present in films. These points motivate a study of Li_2O and Li_2S films.

Such films have been systematically investigated only a few times previously. For Li_2O, Kozen *et al.* prepared dense films using atomic layer deposition (ALD),[11] and Wulfsberg *et al.* used electron microscopy to study lithium metal oxidation,[12] but neither work discussed transport rates. Guo *et al.* grew Li_2O films on Li metal by exposure to oxygen gas and measured a through-plane conductivity of 2×10^{-9} S cm^{-1} at 25 °C.[10] For Li_2S, Meng *et al.* grew XRD-amorphous films by ALD and demonstrated stable battery cycling performance.[13] Klein *et al.* prepared Li_2S films by RF sputtering[14] and estimated the ionic conductivity after annealing at 600 °C to be 10^{-11} S cm^{-1} at 25 °C.[15] It is also worth mentioning two studies that reached different conclusions about the impact of grain size. For Li_2O, Indris *et al.* reported a negligible impact on ionic conductivity from reducing the grain size by ball milling.[16] For Li_2S, Lin *et al.* observed higher conductivity values from nanocrystalline material than from microcrystalline material,[17] but all the values were anomalously low compared to other works on Li_2S (*cf.* Fig. S3 in ref. 9). In a previous work, we explored how changing the deposition parameters affects the morphology of Li_2O and Li_2S films grown by sputter deposition or thermal evaporation.[18] Here we discuss the behavior of sputter-deposited films grown with a dense nanocrystalline morphology. In particular, we focus on in-plane transport measurements, which are a standard method for probing interfacial effects in films[19–21] while avoiding problems with short circuiting that can arise in a through-plane geometry.[22] Experimental details are given in the ESI.†

Fig. 1 shows representative data from the structural characterization of the films. X-ray diffraction (XRD) patterns show only reflections corresponding to polycrystalline Li_2O or Li_2S with a preferred (111) out-of-plane orientation. Raman spectra show only peaks corresponding to Li_2O, Li_2S, and the Al_2O_3 substrate. The polysulfide species discussed in ref. 14 is not

Max Planck Institute for Solid State Research, Heisenbergstraße 1, Stuttgart 70569, Germany. E-mail: r.usiskin@fkf.mpg.de

† Electronic supplementary information (ESI) available: Experimental details, additional transport measurements, SEM images, and references for the data in Fig. 4. See DOI: 10.1039/d1cc00557j

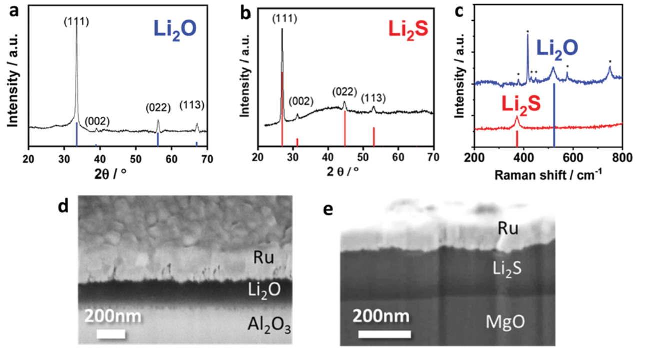

Fig. 1 Typical structural characterization of films grown by sputter deposition. (a and b) X-ray diffraction patterns measured from Li_2O grown on Al_2O_3 and Li_2S grown on MgO. (c) Raman spectra. Asterisks denote Al_2O_3 peaks.[23] (d and e) Focused ion beam–scanning electron microscopy cross-section images, which include the Ru electrodes used for transport measurements. Films were grown from elemental sources in (b–e) and a Li_2O source in (a). In (a–c), the peak positions reported for bulk samples are indicated by vertical lines.[24–27]

observed here, nor is LiOH. In cross-section images, the films appear dense with a fairly uniform thickness.

A schematic of the in-plane configuration used for transport measurements is shown in Fig. S1a (ESI†), and example impedance spectra are shown in Fig. S1b (ESI†). The presence of a low-frequency arc is consistent with blocking of mobile Li^+ at the metal electrodes. The capacitance of the main semicircle corresponds to stray capacitance from the substrate.[28–30] The macroscopic conductivity σ_m extracted from the resistance of the main semicircle is displayed in Fig. 2. As grown, the films of each material show an in-plane conductivity which is higher than that of lightly-doped bulk samples by 3–4 orders of magnitude near room temperature. The values are stable over repeated thermal cycles below the growth temperature, which was 150 °C for Li_2O and 290 °C for Li_2S. The activation energy (determined from the slope of $\sigma_m T$) is 0.5–0.6 eV for the Li_2O films and 0.6 eV for the Li_2S films. For Li_2O, the as-grown conductivity shows some scatter; the data selected for Fig. 2 are representative of the extent of this scatter. A DC measurement performed on a Li_2O film using Li^+-selective electrodes shows a steady current over time (Fig. S2, ESI†), which provides further evidence that the mobile species is Li^+ ions.

The behavior changes markedly upon annealing at higher temperature. After annealing at 340 °C, the films show reduced conductivity values which remain higher than those of 0.1%-doped bulk samples by 1–2 orders of magnitude. The values are stable over repeated thermal cycles from 25–340 °C, and the Li_2O data show less scatter. The activation energy is about 0.85 eV for Li_2O and 0.74 eV for Li_2S. XRD patterns acquired after impedance measurements still show only Li_2O or Li_2S reflections, which rules out significant LiOH formation. Above 340 °C the transport behavior is difficult to assess, because the metal electrodes tend to coarsen and lose adhesion.

To gain further insight, the normalized conductance $\sigma_m L$ after annealing is plotted in Fig. 3 as a function of film thickness. This representation is useful because --- assuming the body of the film has uniform properties --- the intercept obtained by extrapolating to zero thickness corresponds to the excess interfacial contribution.[31] At various temperatures the intercept is indistinguishable from zero, indicating that the conductance after annealing arises from the body of the film, not the interfaces with the substrate or gas phase. This analytical approach could not be used for the as-grown Li_2O data due to scatter, nor for the Li_2S films due to a more limited dataset. However, further investigations of Li_2O show that the conductivity results are largely unaffected when the single crystal substrate is switched from $Al_2O_3(0001)$ to MgO(100), or $MgF_2(001)$, or LiF(111) (Fig. S3, ESI†). These data are strong evidence against a substrate-specific mechanism such as a space charge effect at the film-substrate interface, both before and after annealing. Also, essentially the same transport behavior (and morphology[18]) are observed in films grown from a ceramic Li_2O target instead of elemental Li and O_2 sources (Fig. S3, ESI†).

The transition during annealing is explored in Fig. S4 (ESI†). A useful clue emerges here, in that a mild anneal causes the conductivity to increase before decreasing. In particular, the conductivity of the Li_2O films increases by about a factor of 4 during a mild anneal at 165 °C. The increase persists if the anneal is halted and the temperature lowered. The effect is smaller in Li_2S films, but it still appears. Annealing also leads

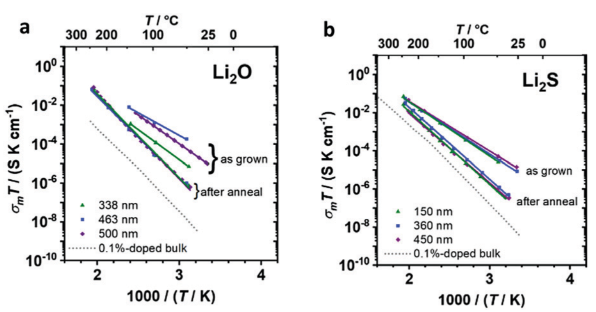

Fig. 2 In-plane macroscopic conductivity of films deposited on single crystal substrates using elemental targets: (a) Li_2O films on $Al_2O_3(0001)$, and (b) Li_2S films on MgO(100). Measurements were acquired both as grown and after annealing at 340 °C. Solid lines are linear fits. Dotted curves correspond to bulk samples of (a) 0.1% LiF-doped Li_2O[8] and (b) 0.1% LiCl-doped Li_2S.[9]

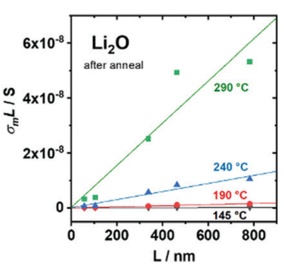

Fig. 3 Thickness dependence of the normalized conductance $\sigma_m L$ after annealing at 340 °C. Films were grown using an elemental Li sputter target. Lines are linear fits.

to grain growth. As grown, the grain size in the Li_2O films is estimated to be 20–50 nm by SEM (Fig. S5, ESI†) and 20 nm by XRD; after annealing at 340 °C, the grain size increases to 50–200 nm by SEM and 60 nm by XRD. Similar findings are seen by SEM for the Li_2S films. More details and representative data are given in ref. 18.

The dominant transport mechanism in the films is unclear. Measurements by XRD, Raman, and SEM show no evidence of an impurity phase. In particular, XRD confirmed the absence of LiOH in multiple films, both before and after impedance measurements. Since the ionic conductivity of bulk LiOH is comparable to that of bulk Li_2O and Li_2S, even if trace LiOH were present, it would not be expected to increase the conductivity.[32] The measured conductivities are also too high to be explained by simple doping of bulk-like Li_2O and Li_2S. The concentration of mobile vacancies does not scale linearly with doping amount at these temperatures due to association effects, so to achieve in bulk samples the conductivity exhibited by the annealed films, dopant concentrations well in excess of 10 mol% (Li_2O) and 1 mol% (Li_2S) would be required.[8,9] To explain the conductivity of the as-grown films, the required concentrations would be even higher. Such high doping levels are implausible, and they were not detected in TOF-SIMS measurements on a Li_2O film, as described in the ESI.† Also, disassociation of defect pairs in doped bulk Li_2O and Li_2S leads to a reversible change in activation energy starting around 130–180 °C (*e.g.*, the dotted curves in Fig. 2 start to bend). This behavior is absent in the annealed films. It is also quite unlikely that the enhanced conductivity is due to high lithium activity, for a few reasons. One, a high lithium activity is not expected, since the films were grown under excess oxygen or sulfur conditions. Two, the ionic defect concentrations in Li_2O and Li_2S are expected from fundamental defect chemistry to be essentially constant over a wide range of lithium activity, due to the predominant ionic disorder. See Fig. 4–8 in ref. 33 for more detail. Three, a high lithium activity would decrease the mobile Li^+ vacancy concentration and the associated conductivity. It would also increase the concentration of interstitial Li^+ ions, but they show a mobility at room temperature which is far too low to account for the observed conduction.[8,9] In short, the film conductivities are inconsistent with bulk-like transport in Li_2O and Li_2S considering only point defects.

Experiments in other material systems offer clues about possible enhancement mechanisms. Consider fluorite CaF_2, which exhibits the same crystal structure as antifluorite Li_2O and Li_2S. In a striking similarity to the present work, evaporated films of CaF_2 show a F^- conductivity that is enhanced by several orders of magnitude relative to lightly-doped bulk CaF_2, and annealing the films at 340 °C yields a decreased enhancement and an increased activation energy.[30,34] Another similarity is that for both CaF_2 and Li_2S films, increasing the growth temperature to 500–600 °C seems to eliminate the enhancement.[18,21] These parallels are strong circumstantial evidence for a similar mechanism. In CaF_2, grain boundaries[35–37] and dislocations[34] have been suggested to provide percolating fast pathways for F^- transport. By analogy, one can hypothesize that grain boundaries and/or dislocations provide fast paths for Li^+ transport in Li_2O and Li_2S, either along the defect cores or in the adjacent space charge zones and strain fields. Consistent with this hypothesis, the Li_2O and Li_2S films exhibit a substantially reduced density of grain boundaries after a 340 °C anneal. The change in activation energy upon annealing could, in principle, be due to a transition from dislocation-driven to grain-boundary-driven conduction and/or a space charge effect with a changing segregation energy. LiI films were also suggested to exhibit fast Li^+ transport along dislocations that anneal out,[38,39] and strong evidence of fast ion conduction along dislocations is available for TiO_2.[40,41] Fast transport along grain boundaries has been observed in several materials.[42] Yet, this behavior is not universal, *e.g.*, nanocrystalline LiF films grown on Al_2O_3 (using the same sputter deposition system as in this work) show a depressed conductivity and disordered structure near the LiF–Al_2O_3 interface.[43]

Alternatively, we cannot entirely rule out the presence of amorphous material. In CaF_2 films grown on Al_2O_3, a few nm-thick amorphous layer was clearly observed at the CaF_2–Al_2O_3 interface by high-resolution transmission electron microscopy (HRTEM); yet, the layer was absent for growth on MgO, and its absence did not appear to substantially affect the conductivity.[30] HRTEM measurements of Li_2O and Li_2S films should be possible in future work using suitable transfer tools. The fact that the conductivity initially increases during annealing (Fig. S4, ESI†) excludes a simple mechanism based on a fast-conducting amorphous phase that crystallizes. However, fast ion transport at amorphous–crystalline interfaces is possible, and the density of those interfaces can initially increase during crystallization, as suggested in the LiF–SiO_2,[29] AgI–Ag_2O–V_2O_5,[44] and $LiAlSiO_4$[45] systems. In all the mechanisms discussed in the last two paragraphs, the higher-dimensional defects percolate along the film, and the local conductivity varies spatially, with regions in proximity to the relevant defects showing a higher conductivity than the measured macroscopic value.

Let us compare the conductivities in this work with those reported for multiphase SEI layers and single-phase samples of common SEI components. For multiphase SEI layers from liquid carbonate electrolytes, Peled gave a typical resistance of 10–1000 Ω cm^2 at 25 °C, which corresponds to 10^{-9}–10^{-7} S cm^{-1} if a thickness of 10 nm is assumed.[1] Guo *et al.* measured 5×10^{-10} S cm^{-1}.[10] For SEI layers from solid sulfide electrolytes, Wenzel *et al.* observed 10–5000 Ω cm^2, or 2×10^{-10}–10^{-7} S cm^{-1} assuming a 10 nm thickness. A similar range of values was observed by Sakuma *et al.*[46] Despite uncertainty about the precise SEI thickness, these data suggest that typical SEI layers containing Li_2O or Li_2S show an overall ionic conductivity on the order of 10^{-10}–10^{-7} S cm^{-1} at 25 °C. Fig. 4 compares this range to the ionic conductivity values at 25 °C measured by impedance spectroscopy from single-phase samples of common SEI constituents. Interestingly, none of the data from the individual bulk materials are consistent with the range of conductivities estimated for the multiphase SEI layers. On the other hand, the films in this work show macroscopic conductivities at 25 °C of 10^{-10}–10^{-7} S cm^{-1} (Li_2O) and 10^{-10}–3×10^{-8} S cm^{-1} (Li_2S), depending on annealing,

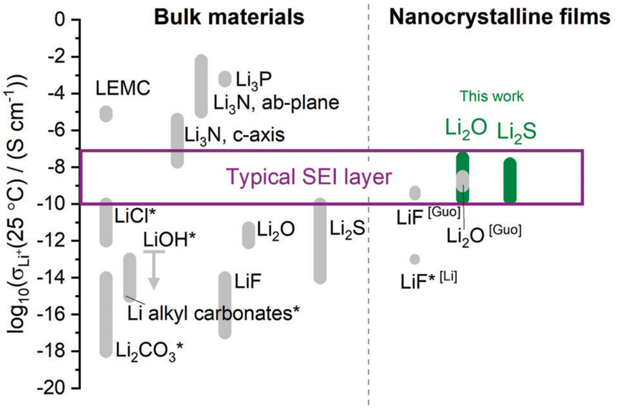

Fig. 4 Ionic conductivity at 25 °C of typical materials in SEI passivation layers, as measured from single-phase bulk or film samples by impedance spectroscopy in this work (green) or in the literature (gray). In many works a range of values has been measured, *e.g.*, depending on doping. An asterisk indicates the values were estimated by extrapolation from data acquired at 100–300 °C and higher. For LiOH an upper bound is shown. Multiphase SEI layers containing Li_2O or Li_2S typically exhibit an ionic conductivity in the range shown (purple). See Tables S1 and S2 (ESI†) for references. LEMC is lithium ethylene monocarbonate. Adapted with permission from ref. 47.

which do agree with the SEI range. This crude comparison considers only the macroscopic ionic conductivities, and it deserves refinement in future work. Nevertheless, it suggests that higher-dimensional defects and interfaces associated with Li_2O and Li_2S may explain the Li^+ transport mechanism in various SEI layers.

We are thankful for support from Dieter Fischer (XRD, Raman), Florian Kaiser (mechanical design), Bernhard Fenk (FIB-SEM), and Tolga Acatürk (SIMS). K. N. gratefully acknowledges financial support from the Masason Foundation.

Open Access funding provided by the Max Planck Society.

Conflicts of interest

There are no conflicts to declare.

Notes and references

1 E. Peled and S. Menkin, *J. Electrochem. Soc.*, 2017, **164**(7), A1703–A1719.
2 S. Wenzel, S. J. Sedlmaier, C. Dietrich, W. G. Zeier and J. Janek, *Solid State Ionics*, 2018, **318**, 102–112.
3 W. Huang, P. M. Attia, H. Wang, S. E. Renfrew, N. Jin, S. Das, Z. Zhang, D. T. Boyle, Y. Li, M. Z. Bazant, B. D. McCloskey, W. C. Chueh and Y. Cui, *Nano Lett.*, 2019, **19**(8), 5140–5148.
4 J. Cabana, L. Monconduit, D. Larcher and M. R. Palacín, *Adv. Mater.*, 2010, **22**(35), E170–E192.
5 C. Xia, C. Y. Kwok and L. F. Nazar, *Science*, 2018, **361**(6404), 777–781.
6 V. Giordani, D. Tozier, J. Uddin, H. J. Tan, B. M. Gallant, B. D. McCloskey, J. R. Greer, G. V. Chase and D. Addison, *Nat. Chem.*, 2019, **11**(12), 1133–1138.
7 P. G. Bruce, S. A. Freunberger, L. J. Hardwick and J. M. Tarascon, *Nat. Mater.*, 2012, **11**(1), 19–29.
8 S. Lorger, R. Usiskin and J. Maier, *J. Electrochem. Soc.*, 2019, **166**(10), A2215–A2220.
9 S. Lorger, R. Usiskin and J. Maier, *Adv. Funct. Mater.*, 2019, **29**, 1807688.
10 R. Guo and B. M. Gallant, *Chem. Mater.*, 2020, **32**(13), 5525–5533.
11 A. C. Kozen, A. J. Pearse, C. F. Lin, M. A. Schroeder, M. Noked, S. B. Lee and G. W. Rubloff, *J. Phys. Chem. C*, 2014, **118**(48), 27749–27753.
12 S. M. Wulfsberg, B. E. Koel and S. L. Bernasek, *Surf. Sci.*, 2016, **651**, 120–127.
13 X. B. Meng, D. J. Comstock, T. T. Fister and J. W. Elam, *ACS Nano*, 2014, **8**(10), 10963–10972.
14 M. J. Klein, G. M. Veith and A. Manthiram, *J. Am. Chem. Soc.*, 2017, **139**(31), 10669–10676.
15 M. J. Klein, G. M. Veith and A. Manthiram, *J. Am. Chem. Soc.*, 2017, **139**(27), 9229–9237.
16 S. Indris, P. Heitjans, H. E. Roman and A. Bunde, *Phys. Rev. Lett.*, 2000, **84**(13), 2889–2892.
17 Z. Lin, Z. C. Liu, N. J. Dudney and C. D. Liang, *ACS Nano*, 2013, **7**(3), 2829–2833.
18 S. Lorger, D. Fischer, R. Usiskin and J. Maier, *J. Vac. Sci. Technol., A*, 2019, **37**(6), 11.
19 C. L. Li and J. Maier, *Solid State Ionics*, 2012, **225**, 408–411.
20 D. Pergolesi, E. Fabbri, S. N. Cook, V. Roddatis, E. Traversa and J. A. Kilner, *ACS Nano*, 2012, **6**(12), 10524–10534.
21 N. Sata, K. Eberman, K. Eberl and J. Maier, *Nature*, 2000, **408**(6815), 946–949.
22 N. J. Dudney, *J. Vac. Sci. Technol., A*, 1998, **16**(2), 615–623.
23 M. Kadleíková, J. Breza and M. Veselý, *Microelectron. J.*, 2001, **32**(12), 955–958.
24 T. W. D. Farley, W. Hayes, S. Hull, M. T. Hutchings and M. Vrtis, *J. Phys.: Condens. Matter*, 1991, **3**(26), 4761–4781.
25 E. Zintl, A. Harder and B. Dauth, *Z. Angew. Chem.*, 1934, **40**, 588–593.
26 Y. Ishii, T. Nagasaki, N. Igawa, H. Watanabe and H. Ohno, *J. Am. Ceram. Soc.*, 1991, **74**(9), 2324–2326.
27 T. A. Yersak, T. Evans, J. M. Whiteley, S. B. Son, B. Francisco, K. H. Oh and S. H. Lee, *J. Electrochem. Soc.*, 2014, **161**(5), A663–A667.
28 M. Gerstl, E. Navickas, G. Friedbacher, F. Kubel, M. Ahrens and J. Fleig, *Solid State Ionics*, 2011, **185**(1), 32–41.
29 C. L. Li, L. Gu and J. Maier, *Adv. Funct. Mater.*, 2012, **22**(6), 1145–1149.
30 R. Usiskin, W. Sigle, M. Kelsch, P. A. Van Aken and J. Maier, in preparation.
31 J. Maier, *Physical Chemistry of Ionic Materials: Ions and Electrons in Solids*, Wiley, 2004.
32 R. T. Johnson, R. M. Biefeld and J. D. Keck, *Mater. Res. Bull.*, 1977, **12**(6), 577–587.
33 J. Maier, *Angew. Chem., Int. Ed.*, 2013, **52**(19), 4998–5026.
34 F. A. Modine, D. Lubben and J. B. Bates, *J. Appl. Phys.*, 1993, **74**(4), 2658–2664.
35 W. Puin, S. Rodewald, R. Ramlau, P. Heitjans and J. Maier, *Solid State Ionics*, 2000, **131**(1-2), 159–164.
36 P. Jain, S. Kim, R. E. Youngman and S. Sen, *J. Phys. Chem. Lett.*, 2010, **1**(7), 1126–1129.
37 G. Scholz, K. Meyer, A. Duvel, P. Heitjans and E. Kemnitz, *Z. Anorg. Allg. Chem.*, 2013, **639**(6), 960–966.
38 D. Lubben and F. A. Modine, *J. Appl. Phys.*, 1996, **80**(9), 5150–5157.
39 E. Schreck, K. Lauger and K. Dransfeld, *Z. Phys. B: Condens. Matter*, 1986, **62**(3), 331–334.
40 K. K. Adepalli, M. Kelsch, R. Merkle and J. Maier, *Adv. Funct. Mater.*, 2013, **23**(14), 1798–1806.
41 K. K. Adepalli, M. Kelsch, R. Merkle and J. Maier, *Phys. Chem. Chem. Phys.*, 2014, **16**(10), 4942–4951.
42 G. Gregori, R. Merkle and J. Maier, *Prog. Mater. Sci.*, 2017, **89**, 252–305.
43 C. L. Li, X. X. Guo, L. Gu, D. Samuelis and J. Maier, *Adv. Funct. Mater.*, 2011, **21**(15), 2901–2905.
44 S. Adams, K. Hariharan and J. Maier, *Solid State Ionics*, 1995, **75**, 193–201.
45 B. Roling and S. Murugavel, Z. Phys. Chemie-Int. J. Res., *Phys. Chem. Chem. Phys.*, 2005, **219**(1), 23–33.
46 M. Sakuma, K. Suzuki, M. Hirayama and R. Kanno, *Solid State Ionics*, 2016, **285**, 101–105.
47 R. Usiskin, Y. Lu, J. Popovic, M. Law, P. Balaya, Y.-S. Hu and J. Maier, *Nat. Rev. Mater.*, 2021, DOI: 10.1038/s41578-021-00324-w.